The Astrophysical Journal Supplement Series, 264:15 (4pp), 2023 January https://doi.org/10.3847/1538-4365/aca7c3

RELICS: A Strong-lens Model of SMACS J0723.3-7327*

Keren Sharon[1], Mandy C. Chen[2], Guillaume Mahler[1], and Dan Coe[3]
(RELICS: Reionization Lensing Cluster Survey)
[1] Department of Astronomy, University of Michigan, 1085 S. University Ave, Ann Arbor, MI 48109, USA; kerens@umich.edu
[2] Department of Astronomy and Astrophysics, The University of Chicago, Chicago, IL 60637, USA
[3] Space Telescope Science Institute, 3700 San Martin Drive, Baltimore, MD 21218, USA
Received 2022 August 15; revised 2022 November 28; accepted 2022 November 29; published 2022 December 23

Abstract

We present the details of a strong-lens model of SMACS J0723.3-7327, which was made public as part of the data and high-level science products (HLSP) release of the RELICS Hubble Space Telescope (HST) treasury program (Reionization Lensing Cluster Survey; GO-14096, PI: Coe). The model products were made available on the Mikulski Archive for Space Telescopes via 10.17909/T9SP45 in 2017. Here, we provide the list of constraints that were used in the HST-based RELICS lens model, as well as other information related to our modeling choices, which were not published with the data and HLSP release. This model was computed with `Lenstool`, used a total of 25 multiple images of eight sources, with no spectroscopic redshifts. The image-plane rms was 0.″58.

Unified Astronomy Thesaurus concepts: Gravitational lensing (670); Galaxy clusters (584)

1. Introduction

The strong-lensing cluster SMACS J0723.3−7327 was observed as one of the JWST Early Release Observations (ERO) targets, and was revealed to the public in 2022 July (Pontoppidan et al. 2022).

Following the ERO release, the field of SMACS J0723.3−7327 was the subject of a number of publications taking advantage of JWST's capabilities, as well as the depth added by the strong-lensing magnification boost, to study the background universe, identify high-z galaxies, and analyze the foreground cluster. In particular, the ERO prompted computation of strong-lens models based on the new data (Caminha et al. 2022; Mahler et al. 2022; Pascale et al. 2022).

Preceding JWST, SMACS J0723.3−7327 was observed by the Hubble Space Telescope (HST), and its lensing signal analyzed as part of the Reionization Lensing Cluster Survey Treasury program (RELICS; PI: Coe). The RELICS collaboration made all high-level data products available to the community, including reduced images, catalogs, and lens models, via the Mikulski Archive for Space Telescopes (MAST) at doi:10.17909/T9SP45.[4] Product-specific README files were provided, and a full description of the catalogs was given in Coe et al. (2019). However, for a large fraction of the 41 RELICS clusters, the details of the lensing analysis (multiple images, spectroscopic redshifts, and modeling choices) were not published. Here, we provide the community with the details of the HST-based lens model of SMACS J0723.3−7327, which was released as part of the RELICS program in 2017, in order to provide context for the public model outputs and facilitate comparisons to the new JWST-based models.

This modeling analysis assumed a flat cosmology with $\Omega_\Lambda = 0.7$, $\Omega_m = 0.3$, and $H_0 = 70$ km s^{-1} Mpc^{-1}. In this cosmology, $1'' = 5.27$ kpc at the cluster redshift, $z = 0.388$, which we rounded to $z = 0.39$.

2. Data

This work used HST mosaics that were produced by the RELICS collaboration, combining archival imaging obtained with the Advanced Camera for Surveys (ACS)/F606W (1200 s, GO-12166) and ACS/F814W (1440 s, GO-12884), with the new RELICS imaging (GO-14096) taken with ACS/F435W (2233 s), F606W (1089 s), F814W (1089 s), and WFC3-IR/F105W (6059 s), F125W (3248 s), F140W (5234 s), and F160W (4523 s). The depth in each filter varies between 0.5 and 2 orbits. For details of the observations, data reduction, photometric and photo-z catalogs we refer the reader to Coe et al. (2019) and references therein. In short, raw images were corrected for bias and dark current, and flat-fielded using the standard STScI pipeline; ACS images were corrected for charge-transfer efficiency and bias striping, and combined while rejecting cosmic rays, bad pixels, and other artifacts. The images in each filter were then aligned and drizzled onto a common pixel grid with 0.″03 px^{-1} and 0.″6 px^{-1} using AstroDrizzle (Gonzaga et al. 2012), taking into account the correlated pixel noise and Poisson source noise of each pixel as weights. Finally, the astrometry was linked to the Wide-field Infrared Survey Explorer point-source catalog (Wright et al. 2010).

3. Lensing Analysis

3.1. Multiple Images

Composite color images of the field were visually inspected to identify instances of multiple images of the same background-lensed sources, to be used as lensing constraints. As is common procedure (e.g., Sharon et al. 2020) we proceeded to build the lens model iteratively, starting with the most obvious and secure identification, and using preliminary iterations of the

* Based on observations made with the NASA/ESA Hubble Space Telescope, obtained at the Space Telescope Science Institute, which is operated by the Association of Universities for Research in Astronomy, Inc., under NASA contract NAS 5-26555. These observations are associated with programs GO-12166, GO-12884, GO-14096.
[4] https://archive.stsci.edu/prepds/relics/

Table 1
List of Lensing Constraints

ID	R.A. (deg) J2000	Decl. (deg) J2000	Model-z
Source 1:			[2.2]
1.1	110.80504	−73.454536	
1.2	110.80681	−73.458358	
1.3	110.81306	−73.448694	
Source 2:			$1.29^{+0.09}_{-0.14}$
2.1	110.84047	−73.450975	
2.2	110.84270	−73.454747	
2.3	110.83876	−73.458692	
Source 3:			$2.01^{+0.13}_{-0.23}$
3.1	110.82491	−73.459581	
3.2	110.83152	−73.455153	
3.3	110.83019	−73.448453	
3.4	110.82297	−73.454786	
Source 4:			$1.36^{+0.04}_{-0.13}$
4.1	110.82364	−73.451800	
4.2	110.82210	−73.452686	
4.3	110.82067	−73.460128	
Source 5:			$1.99^{+0.17}_{-0.22}$
5.1	110.82522	−73.459686	
5.2	110.83176	−73.455108	
5.3	110.83027	−73.448542	
5.4	110.82316	−73.454736	
Source 6:			$3.23^{+0.63}_{-0.44}$
6.1	110.83212	−73.454375	
6.2	110.82170	−73.454108	
6.3	110.82948	−73.448914	
6.4	110.82289	−73.461631	
Source 7:			$1.65^{+0.28}_{-0.19}$
7.1	110.83560	−73.451735	
7.2	110.83652	−73.453005	
Source 8:			$1.23^{+0.08}_{-0.11}$
8.1	110.83842	−73.451014	
8.3	110.83610	−73.458784	

Note. The coordinates match the world coordinate system solution of the RELICS data reduction version `v1`, which is available on MAST.

lens model to identify new constraints. We identified eight sets of multiply imaged sources (Table 1, Figure 1), belonging to seven unique sources (the sources labeled 3 and 5 may be associated with the same galaxy). At the time of the computation of the model, none of the lensed sources had spectroscopic redshifts. We obtained photometric redshifts based on the extensive HST imaging, using the Bayesian Photometric Redshifts (Benitez 2000) algorithm (see Cerny et al. 2018; Coe et al. 2019; Salmon et al. 2020).

3.2. Lens-model Components

We modeled the cluster using the public software `Lenstool` (Jullo et al. 2007). This algorithm uses MCMC formalism to explore the parameter space and identify the best-fit set of parameters, which minimize the scatter between the observed and predicted lensing evidence. The cluster component was represented by a parametric pseudoisothermal mass distribution halo (PIEMD, a.k.a. dPIE; Elíasdóttir 2007), with parameters x, y, e, θ, $r_{\rm core}$, $r_{\rm cut}$, and σ. All the parameters were allowed to vary within broad priors, except for $r_{\rm cut} = 1000$ kpc. Another PIEMD halo represented the brightest cluster galaxy (BCG), with x, y, e, and θ fixed to the observed values as measured with Source Extractor (Bertin & Arnouts 1996) in the F814W image, and the others allowed to vary. We selected cluster-member galaxies based on their color in a F606W–F814W versus F814W diagram using the red-sequence technique (Gladders & Yee 2000). To measure magnitudes and colors, we used Source Extractor (Bertin & Arnouts 1996) in dual-image mode with the F814W band used for reference and photometry. Stars were identified and removed from the catalog based on their location in a `MU_MAX` versus `MAG_AUTO` diagram. Galaxies that were selected as cluster members were included as PIEMD halos in the model. The positional parameters of the galaxies were fixed to their catalog values, whereas $r_{\rm core}$, $r_{\rm cut}$, and σ were determined by `Lenstool` based on the scaling relations that are described in Limousin et al. (2005), with pivot parameters `mag0` = 19.12 mag and `corekpc` = 0.15 kpc; the scaling relation parameters `sigma` and `cutkpc` were optimized by the model. The model used a total of 145 halos, of which two were individually optimized. Table 2 tabulates the model components and best-fit parameters.

We fixed the redshift of Source 1 to the its photometric redshift, $z_{\rm phot} = 2.2$. The redshifts of all the other lensed sources were entered as free parameters with broad flat priors ($0.5 < z < 5$). The broad priors were used in order to not be affected by possible catastrophic photo-z outliers. Some photo-z measurements exhibited large uncertainties, or gave inconsistent results for multiple images of the same source. This was in part due to contamination from other sources (e.g., images of Sources 3 and 5 are projected near a bright star). Other than fixing one redshift to the most secure photo-z, we only used the photo-z information statistically, to check that overall the lens-model predictions are consistent with the photometric redshifts (see Cerny et al. 2018 for a description of this approach). The diagnostic plot of model-z versus photo-z is shown in the bottom-right panel of Figure 1.

Including the free redshifts, this model has a total of 18 free parameters (six for the cluster halo, three for the BCG halo, two for cluster-member galaxies scaling, and seven free redshifts), and 34 constraints (25 images from eight sources).

4. Results

The observed images of lensed sources were reproduced well by the lens model, with a typical image-plane scatter per system of $<0\farcs5$. A somewhat higher image-plane scatter for System 2 drove the overall image-plane rms to $0\farcs58$. Figure 1 shows the lensing constraints and the best-fit critical curve for a source at $z = 3$, overplotted on the HST imaging. The bottom-right panel of Figure 1 shows a comparison of the model-predicted redshift and the photometric redshifts measured by RELICS. As noted above, this plot was used as a diagnostic tool to assess the model, in lieu of spectroscopic redshifts. We found that overall the model did not appear to systematically overpredict or underpredict the photometric redshifts.

Spectroscopic redshifts were not available at the time this model was computed, but were recently published by several authors (Golubchik et al. 2022; Mahler et al. 2022), based on data obtained by the Multi Unit Spectroscopic Explorer on the Very Large Telescope. We compare the spectroscopic redshifts from Mahler et al. (2022) to the posterior distributions of the free redshifts of systems 2–8 (the redshift of System 1 was fixed to its photo-z, $z_{\rm phot} = 2.2$, which does not have a spectroscopic redshift). The best-fit redshift of each system is indicated in orange, and the spectroscopic redshift in blue. We find that the model correctly predicted the redshift(s) of

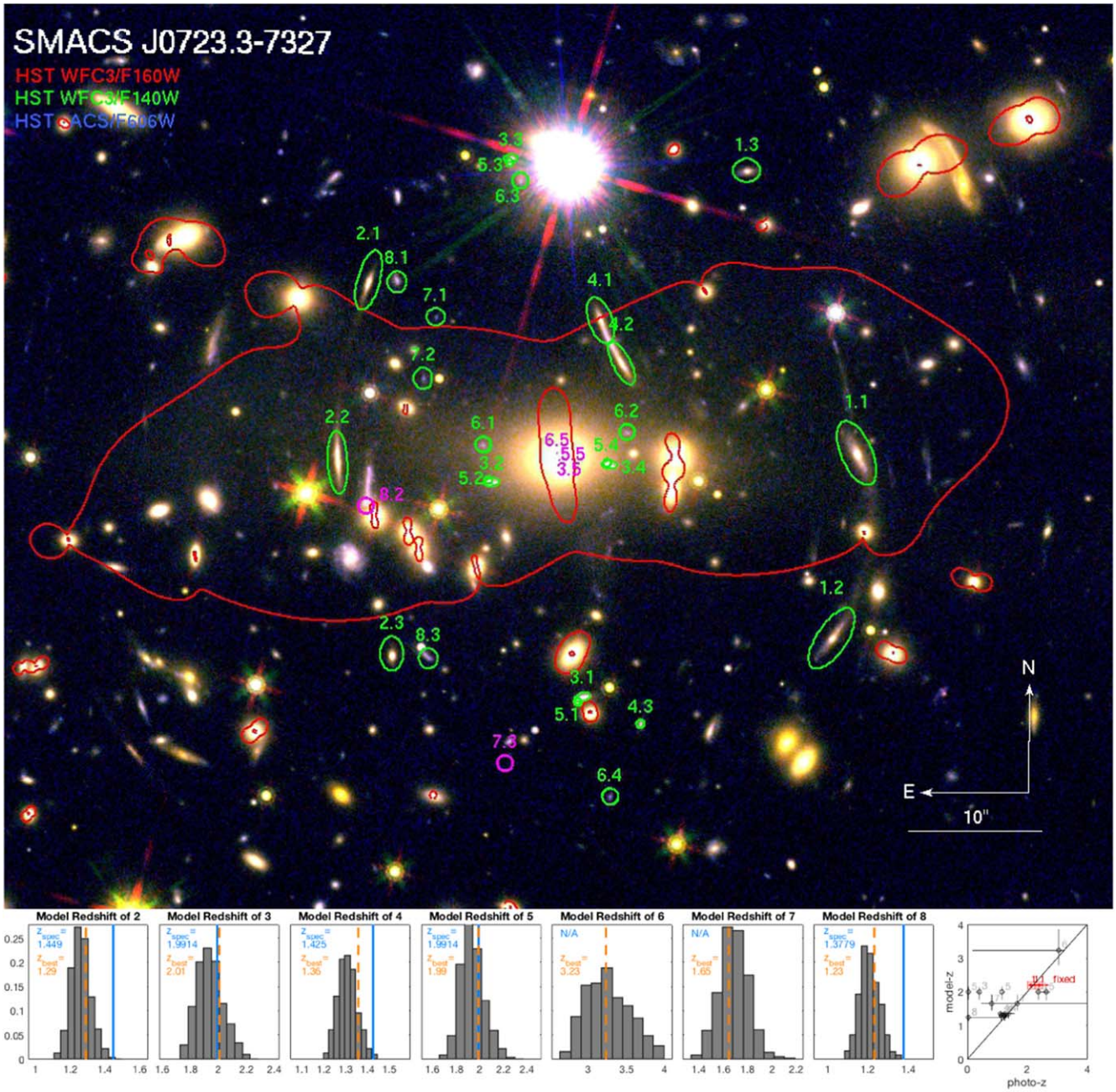

Figure 1. Top: HST imaging of SMACS J0723.3−7327 in WFC3-IR/F160W, WFC3-IR/F140W, and ACS/F606W. The eight multiple-image sets that were used to constrain the RELICS model are overplotted and labeled in green. Model-predicted counter images that were not used as constraints are plotted in magenta. The critical curves for a source at $z = 3$ are shown in red. Bottom: the posterior distribution of source redshifts for sources 2–8 are shown in gray histograms (Source 1 was fixed to its photo-z, $z_{\rm phot} = 2.2$). The orange dashed line points to the best-fit model prediction. Solid blue lines mark the recently published spectroscopic redshifts from Mahler et al. (2022), which were not available at the time this model was computed (see also Golubchik et al. 2022). The rightmost panel compares the model redshift to the photometric redshifts from RELICS; this plot was used as a diagnostic tool in the modeling process. The coordinates of the lensing constraints are tabulated in Table 1.

system(s) 3 and 5, but underpredicted the redshifts of systems 2, 4, and 8 by $\Delta z/(1+z) = 0.065$, 0.027, 0.062, respectively.

The lens model provides a map of the projected mass density, from which we measure the total mass enclosed within several apertures. We find $M(<128\,\mathrm{kpc}) = 80.8 \pm 0.7 \times 10^{12}\,M_{\odot}$, $M(<200\,\mathrm{kpc}) = 146.1 \pm 2.1 \times 10^{12}\,M_{\odot}$, and $M(<200\,\mathrm{kpc}) = 323^{+8}_{-6} \times 10^{12}\,M_{\odot}$. We refer the reader to Mahler et al. (2022) for a comparison between several lensing analyses of this cluster.

RELICS made the following lensing products publicly available through MAST: shear (γ), convergence (κ), lensing potential (ψ), deflection in the x- and y-directions (α_x,α_y), and magnification maps ($\mu(z)$) for several redshifts. With the exception of magnification, the files are scaled to effectively $D_{ls}/D_s = 1$, where D_{ls}, D_s are the angular diameter distances from the lens to the source and from the observer to the source, respectively. They can be rescaled to any source redshift by multiplying by the relevant D_{ls}/D_s. We also made available a set of 100 files of each of the above, sampled from the MCMC chain, which can be used to estimate the statistical uncertainties related to the lens-modeling process.

This paper complements the public models and provides context for current works that aim to take full advantage of the new JWST data, and have either already used the public

Table 2
Best-fit Lens-model Parameters

No.	Component	Δ R.A. (″)	Δ Decl. (″)	e	θ (deg)	$r_{\rm core}$ (kpc)	$r_{\rm cut}$ (kpc)	σ_0 (km s^{-1})
1	Cluster halo	$0.47^{+1.98}_{-1.37}$	$0.86^{+0.25}_{-0.34}$	0.71 ± 0.09	$6.62^{+0.67}_{-0.46}$	$89.9^{+16.9}_{-14.2}$	[1500]	1056^{+45}_{-48}
2	BCG	[0]	[0]	[0.161]	[29.2]	$2.11^{+0.77}_{-2.04}$	$22.8^{+74.8}_{-8.1}$	351^{+24}_{-72}
	L* galaxy	…	…	…	…	…	$53.5^{+15.8}_{-23.0}$	161^{+34}_{-27}

Note. The coordinates are given in arcseconds relative to [R.A., decl.] = [110.826750, −73.454628]. All the mass components are parameterized as PIEMD, with ellipticity expressed as $e = (a^2 - b^2)/(a^2 + b^2)$. θ is measured north of west. Statistical uncertainties are inferred from the Markov Chain Monte Carlo (MCMC) optimization and correspond to a 95% confidence interval. Parameters that were not optimized are listed in square brackets. The location and the ellipticity of the matter clumps associated with cluster galaxies were kept fixed according to their light distribution, and the other parameters determined through scaling relations (see text). The image-plane rms is 0.″58.

models, or wish to compare a JWST-based lensing analyses to the pre-JWST models.

Based on observations with the NASA/ESA HST, obtained at STScI, which is operated by AURA under NASA contract NAS5-26555, associated with the RELICS Treasury Program GO-14096, and with programs GO-12166 and GO-12884. The data were obtained from Mikulski Archive for Space Telescopes (MAST). Support for GO-14096 was provided through a grant from the STScI under NASA contract NAS5-26555. G.M. received funding from the European Union's Horizon 2020 research and innovation programme under the Marie Sklodowska-Curie grant agreement No. 896778.

Facilities: HST(ACS), HST(WFC3), HST(MAST).

Software: `Lenstool` (Jullo et al. 2007), Source Extractor (Bertin & Arnouts 1996), MATLAB Astronomy and Astrophysics Toolbox (MAAT; Ofek 2014).

ORCID iDs

Keren Sharon https://orcid.org/0000-0002-7559-0864
Mandy C. Chen https://orcid.org/0000-0002-8739-3163
Guillaume Mahler https://orcid.org/0000-0003-3266-2001
Dan Coe https://orcid.org/0000-0001-7410-7669

References

Benitez, N. 2000, ApJ, 536, 571
Bertin, E., & Arnouts, S. 1996, A&AS, 117, 393
Caminha, G. B., Suyu, S. H., Mercurio, A., et al. 2022, A&A, 666, L9
Cerny, C., Sharon, K., Andrade-Santos, F., et al. 2018, ApJ, 859, 159
Coe, D., Salmon, B., Bradac, M., et al. 2019, ApJ, 884, 85
Elíasdóttir, A. 2007, arXiv:0710.5636
Gladders, M. D., & Yee, H. K. C. 2000, AJ, 120, 2148
Golubchik, M., Furtak, L. J., Meena, A. K., & Zitrin, A. 2022, ApJ, 938, 14
Gonzaga, S., Hack, W., Fruchter, A., & Mack, J. 2012, The DrizzlePac Handbook
Jullo, E., Kneib, J. P., Limousin, M., et al. 2007, NJPh, 9, 447
Limousin, M., Kneib, J. P., & Natarajan, P. 2005, MNRAS, 356, 309
Mahler, G., Jauzac, M., Richard, J., et al. 2022, arXiv:2207.07101
Ofek, E. O. 2014, MAAT: MATLAB Astronomy and Astrophysics Toolbox, Astrophysics Source Code Library, ascl:1407.005
Pascale, M., Frye, B. L., Diego, J., et al. 2022, ApJL, 938, L6
Pontoppidan, K., Blome, C., Braun, H., et al. 2022, ApJL, 936, L14
Salmon, B., Coe, D., Bradley, L., et al. 2020, ApJ, 889, 189
Sharon, K., Bayliss, M. B., Dahle, H., et al. 2020, ApJS, 247, 12
Wright, E. L., Eisenhardt, P. R. M., Mainzer, A. K., et al. 2010, AJ, 140, 1868